UC Berkeley

UC Berkeley Previously Published Works

Title

City-Scale Building Anthropogenic Heating during Heat Waves

Permalink

https://escholarship.org/uc/item/6bz636wm

Journal

Atmosphere, 11(11)

ISSN

0004-6973

Authors

Luo, Xuan

Vahmani, Pouya

Hong, Tianzhen

et al.

Publication Date

2020

DOI

10.3390/atmos11111206

Peer reviewed

eScholarship.org Powered by the California Digital Library
University of California

atmosphere

MDPI

Article

City-Scale Building Anthropogenic Heating during Heat Waves

Xuan Luo, Pouya Vahmani, Tianzhen Hong * and Andrew Jones

Lawrence Berkeley National Laboratory, Berkeley, CA 94720, USA; xuanluo@lbl.gov (X.L.); pvahmani@lbl.gov (P.V.); adjones@lbl.gov (A.J.)

* Correspondence: thong@lbl.gov

Received: 12 October 2020; Accepted: 4 November 2020; Published: 7 November 2020

Abstract: More frequent and longer duration heat waves have been observed worldwide and are recognized as a serious threat to human health and the stability of electrical grids. Past studies have identified a positive feedback between heat waves and urban heat island effects. Anthropogenic heat emissions from buildings have a crucial impact on the urban environment, and hence it is critical to understand the interactive effects of urban microclimate and building heat emissions in terms of the urban energy balance. Here we developed a coupled-simulation approach to quantify these effects, mapping urban environmental data generated by the mesoscale Weather Research and Forecasting (WRF) coupled to Urban Canopy Model (UCM) to urban building energy models (UBEM). We conducted a case study in the city of Los Angeles, California, during a five-day heat wave event in September 2009. We analyzed the surge in city-scale building heat emission and energy use during the extreme heat event. We first simulated the urban microclimate at a high resolution (500 m by 500 m) using WRF-UCM. We then generated grid-level building heat emission profiles and aggregated them using prototype building energy models informed by spatially disaggregated urban land use and urban building density data. The spatial patterns of anthropogenic heat discharge from the building sector were analyzed, and the quantitative relationship with weather conditions and urban land-use dynamics were assessed at the grid level. The simulation results indicate that the dispersion of anthropogenic heat from urban buildings to the urban environment increases by up to 20% on average and varies significantly, both in time and space, during the heat wave event. The heat dispersion from the air-conditioning heat rejection contributes most (86.5%) of the total waste heat from the buildings to the urban environment. We also found that the waste heat discharge in inland, dense urban districts is more sensitive to extreme events than it is in coastal or suburban areas. The generated anthropogenic heat profiles can be used in urban microclimate models to provide a more accurate estimation of urban air temperature rises during heat waves.

Keywords: anthropogenic heat; building heat emissions; WRF-UCM; urban building energy model; heat wave; urban microclimate

1. Introduction

Extremely high temperatures have occurred globally and concurrently in the past several years. The July 2019 global land and ocean surface temperature's departure from average was the highest for July since global records began in 1880 [1]. The record-hottest month in 2019 precipitated an increase in intensity and frequency of extreme heat events over many regions, including North America, Asia, and Europe [2]. The recurrence and increasing severity of these extreme weather events are becoming a growing concern for city policymakers who must provide critical services to preserve human life and properties during natural disasters [3]. Meanwhile, in urban areas, studies with observational and modeling analyses indicate synergies between urban heat islands (UHIs) and heat waves, when

temperature rise can be exacerbated due to the UHI effect, and consequently intensify the variability of microclimates [4]. Risk analysis and prioritization of mitigation strategies to address these events in cities will require a deep and quantitative understanding of the combined effects of urban microclimate and heat waves [5].

Rapid urbanization is resulting in dramatic land use and energy balance changes. The expansion of built-up areas and concentrated population directly results in a vast energy demand [6]. Urban areas consume between 67% and 76% of all global energy [7], and the total usage will increase more than threefold if current trends in global urban expansion continue [8]. Energy-related human activities are accompanied by the emission of anthropogenic heat (AH) from transportation, industries, and building air-conditioning [9]. Although AH emission itself is not a significant portion of the global energy budget, its implications for urban microclimate and UHI can be significant [10]. Recent research has suggested that human-induced climate change contributes to the occurrence of extraordinary global-scale heat waves [11]. With the substantial increase of urban population and frequency of extreme weather events, the concerns of heat-related health risks underline the importance to study the interactive effects of urban microclimate and AH in terms of the urban energy balance.

Major sources of urban AH include the waste heat dispersion from vehicles, buildings (e.g., from building heating, ventilation, and air-conditioning (HVAC) systems), industry, and human metabolism [12]. Among them, waste heat from vehicles, industries, and humans are relatively less affected by variations in weather, while heat emissions from buildings vary diurnally and seasonally, depending on local weather conditions. In 2015, Sailor et al. published a national AH database with profiles aggregated from human metabolism, vehicles, and buildings, including heat rejected directly from electricity consumption and fuel combustion [10]. Averaged over cities, building electricity and heating fuel use contribute to 50% to 65% of the AH among those three components for different months in a year. Sun et al. adopted a similar inventory approach for quantifying temporal-spatial patterns of AH in Beijing, and the results showed that residential and commercial buildings account for 45% of the total AH fluxes, followed by traffic (30%), industrial (20%), and human metabolism (5%) [13]. Overall, AH from the building sector comprises a major proportion of the total profiles but is more difficult to estimate and predict due to its correlation with urban morphology, weather, occupancy, and technology adoption.

Building heat emissions into the atmosphere can be emitted directly from air exchange or directly from heat transfer between the building and outdoor environment. Air exchange includes exiting air through exfiltration, ventilation, and relief air from heating and cooling systems. Indirect heat emission includes radiative and convective heat transfer between the building envelope and ambient air due to temperature differences, and rejected heat from electricity use and fuel combustion [14]. Although commonly simplified as building energy use, research studies have demonstrated that actual AH released from buildings can differ substantially from energy consumption in magnitude and time latency [14–16]. The impact of building heat emissions on urban microclimates has been studied from building to city scales. Nie et al. investigated the impacts of AH on summertime rainfall in Beijing using a building energy model (BEM) incorporated into the Weather Research and Forecasting (WRF) model system, and demonstrated that AH from buildings enhances mixing and turbulent energy transport, which consequently enhances urban rainfall and may also modify the spatial pattern of the rainfall [17]). Bohnenstengel et al. derived AH flux from energy demand data for London, including variations on diurnal and seasonal timescales, and concluded that the AH flux increases the UHI by 1 K in May and 1.5 K in December [18]. Ohashi et al. estimated the released waste heat as building energy consumption simulated from a BEM in the office areas in Tokyo. Coupled with an urban canopy meteorological model (CM), the simulation results indicated the waste heat from the air conditioners caused a temperature rise of 1 °C to 2 °C or more on weekdays in the Tokyo office areas [19]. Another study in Tokyo also found that AH in central Tokyo could lead to an increase in nocturnal air temperature of above 2 °C in winter and 1.5 °C in summer [20].

Among the reviewed articles, three main approaches were commonly used to quantify building waste heat dispersion: (1) assessment with inventory approaches, (2) assessment through heat energy balances, and (3) assessment through physics-based modeling of building energy systems and simulations [14]. The inventory method uses spatially explicit data related to features such as the building typology, district demographics, and population density. This is the most widely used method, as the needed data are easy to acquire. The energy balance assessment method examines the energy entering and exiting the domain, and commonly uses measurement data to quantify the overall heat discharge to the atmosphere. However, both methods have less flexibility in measuring the diurnal dynamics of heat emission profiles under various weather events. The third method, applying bottom-up physics models, has the advantage of using weather conditions as inputs, and also allows the representation of high temporal resolution results as feedback to weather or microclimate simulations. Building energy models are able to assess building performance for space heating and cooling and ventilation by considering internal loads and system efficiency variabilities under different environmental boundary conditions [14]. The approach also makes it possible to easily evaluate modeling hypotheses and the sensitivity of different climate variables and scenarios [21].

There have been many large-scale analyses of the impact of AH in microclimate modeling and simulation studies. However, the temporal variability and sensitivity to the extreme weather events of AH fluxes have not been adequately studied. Most commonly, two-dimensional statistical heat fluxes from buildings are aggregated with spatial distributions, fed as the input of static simulations with urban heat balance equations to analyze the sensitivity of regional weather to AH [22–25]. Other climate models (those coupled with urban canopy models) consider heat emissions from buildings as a diurnal profile based on pre-assumed waste heat inventories [26,27] or collected energy statistics. The coupling improves the fidelity of considering the feedback from AH to the local climate, yet the statistical aggregations of heat fluxes and the static simulation under certain scenarios do not reflect the temporal variabilities of AH under various weather events. In mesoscale, simulations that couple BEM with higher fidelity urban climate models allow users to compute the heat released into the atmosphere by air-conditioning facilities, as well as the corresponding feedback to different meteorological variables. Chow et al. adopted a simplified BEM, treating urban blocks as a pile of boxes, and calculated the waste heat generated by the electrical consumption of the air-conditioning (AC) [28]. Imported to WRF, the results indicated that local-scale nocturnal urban temperatures can be increased by 1 °C due to AC use in an extreme heat event in the Phoenix, Arizona, metropolitan area. Another study coupled simulation between a BEM and Urban Canopy Parameterizations (UCP) in an idealized fictional urban area and observed that heat from wall ACs leads to mean near-ground temperature difference, rising in base-case conditions from 0.4 °C to 1.2 °C. These approaches lack realistic BEM models, considering the complexity of urban morphologies and building geometries, and raise discussions of weighing model fidelity over the ability to scale. They also use building energy use in the coupled simulation instead of the actual hourly heat fluxes discharge. Overall, to quantify the interacting effects of microclimate and building waste heat discharge under certain extreme weather events, a co-simulation approach is recommended, with (1) a high-resolution microclimate simulation, (2) a high-resolution building heat emission simulation with building energy modeling, and (3) a data exchange to consider the two-way dynamic interactions.

This study aimed to develop an approach to quantify the AH from buildings using a bottom-up simulation approach under extreme heat events at the city scale. We demonstrated the approach with a case study in the city of Los Angeles, California, monitoring a five-day heat wave event in September 2009, and analyzed the environmental temperature rise and energy use surge during the event. High-resolution meteorological data were generated by the mesoscale WRF coupled to Urban Canopy Model (WRF-UCM). Grid level weather files were first derived from the simulation results of the WRF-UCM, running at a high-resolution (500 m by 500 m). We then simulated and aggregated the grid level building heat emission profiles using prototype EnergyPlus building energy models with collected urban land use and urban building density data. The results are presented as clustered

diurnal profiles as potential feedbacks of the WRF-UCM model. We also analyzed the spatial patterns of anthropogenic heat discharge from the building sector and evaluated the quantitative relationship to weather conditions and urban land-use dynamics at the grid scale.

2. Data and Methods

2.1. Area of Focus

We chose the city of Los Angeles (LA), California, as the study area. As one of the most populous urban areas in the United States, LA city held almost four million people as of 1 July 2015 [29]. Los Angeles has a Subtropical-Mediterranean climate (Köppen climate classification) and has dry and hot summers and moist winters. It is an urban heat island due to its dense population, and has microclimates with variations in temperature and humidity from its coastal areas to its inland areas. Recent studies identified building energy consumption as the dominant contributor to the AH in LA [30]. The building heat emissions in the downtown area were found to be the most significant throughout the year among all the city's neighborhoods, and were more significant on workdays than on non-workdays.

2.2. Description of the WRF Model Set Up

To capture the urban microclimate dynamics under extreme heat conditions, we employed the widely used WRF-UCM modeling framework, which consisted of a mesoscale meteorological model (WRF) dynamically coupled to an urban canopy model (UCM) [31,32]. WRF is a state-of-the-science, fully compressible, non-hydrostatic, mesoscale numerical weather prediction model. A nested domain configuration was used for WRF to downscale climate dynamics to a resolution (500 m) that is relevant to urban processes (Figure 1). The UCM, incorporated in the land surface model in WRF, resolves urban canopy processes [31,32] and surface energy balance for urban surfaces, accounting for the three-dimensional nature of urban surfaces, as well as shadowing, reflections, radiation trapping, and wind profiles inside a street canyon [33].

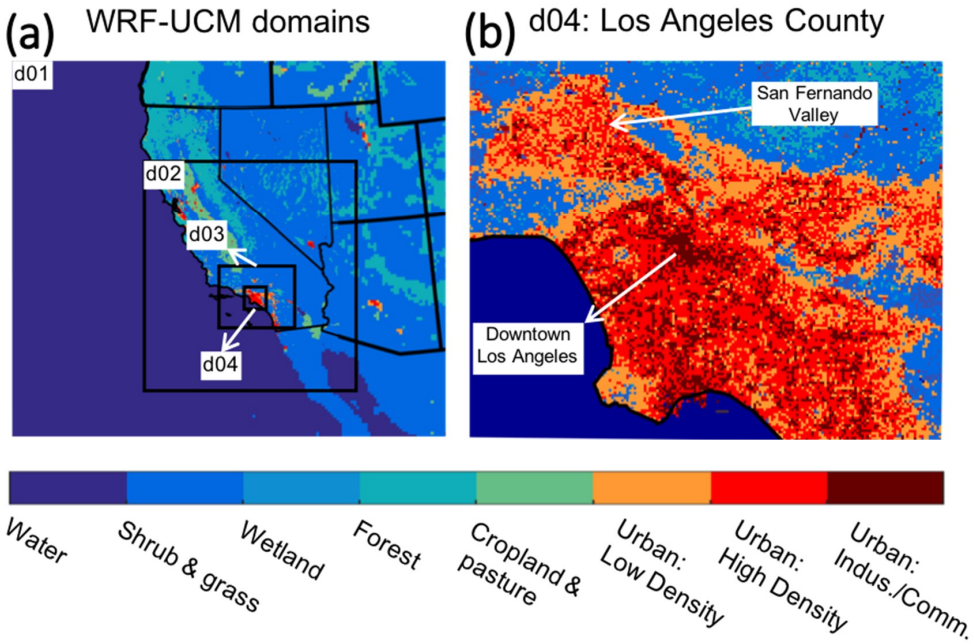

Figure 1. WRF-UCM domain configuration: (**a**) four nested domains with horizontal resolutions of 13.5, 4.5, 1.5, and 0.5 km for d01, d02, d03, and d04, respectively; (**b**) the innermost domain (d04), covering urban Los Angeles county with a 500 m resolution.

We used WRF-UCM (version 4.1.2) [34,35] over four two-way nested domains with horizontal resolution of 13.5 km (km) (domain 1), 4.5 km (domain 2), 1.5 km (domain 3), and 0.5 km (domain 4), and 30 atmospheric levels in the vertical (Figure 1). The parametrizations for the physical processes in the WRF-UCM included the Morrison double moment scheme [35] for microphysics, Dudhia scheme [36] for shortwave radiation, Rapid Radiative Transfer Model [37] for longwave radiation, University of Washington (TKE) Boundary Layer Scheme [38] for the planetary boundary layer, Grell–Freitas scheme [39] for cumulus parameterization (in domains 1 and 2 only), and Eta Similarity scheme [40] for the surface layer. We used high-resolution (30 m) National Land Cover Data (NLCD) [41] for an accurate representation of urban land use/land cover type. We also used the NLCD impervious surface data [42] to define the impervious (or urban) fraction, which divides urban grid cells into pervious (undeveloped) and impervious (developed) fractions. We further used the National Urban Database and Access Portal Tool [16] dataset in the WRF-UCM framework for a realistic and domain-specific representation of urban morphology such as building height, road and roof width. The performance of described configuration of WRF-UCM has been validated over the Los Angeles metropolitan area against ground observation of meteorological conditions in previous studies [43]. These studies show a reasonable model performance over the region, predicting daily mean and maximum air temperatures with RMSDs of 1.1 °C and 0.4 °C, respectively.

2.3. Identification of the Heat Wave Event

We used 15-year simulations conducted with WRF-UCM to identify a high-impact heat wave over Los Angeles county. We adopted a widely used universal threshold of 35 °C [43–46] to identify extreme heat days (i.e., a day with maximum air temperature of 35 °C or higher). A heat wave consists of at least three consecutive extreme heat days. We identified 12 high-impact heat waves between 2001 and 2015, as heat waves that impact most (>800 square kilometers (km^2)) of urban Los Angeles county (Figure 2). In this study, we particularly focused on the 22 September 2009, heat wave as it maintained a high intensity over an extended period of time, which represents the characteristics of mid-century heat waves under a changing climate, as reported by Vahmani et al. [43].

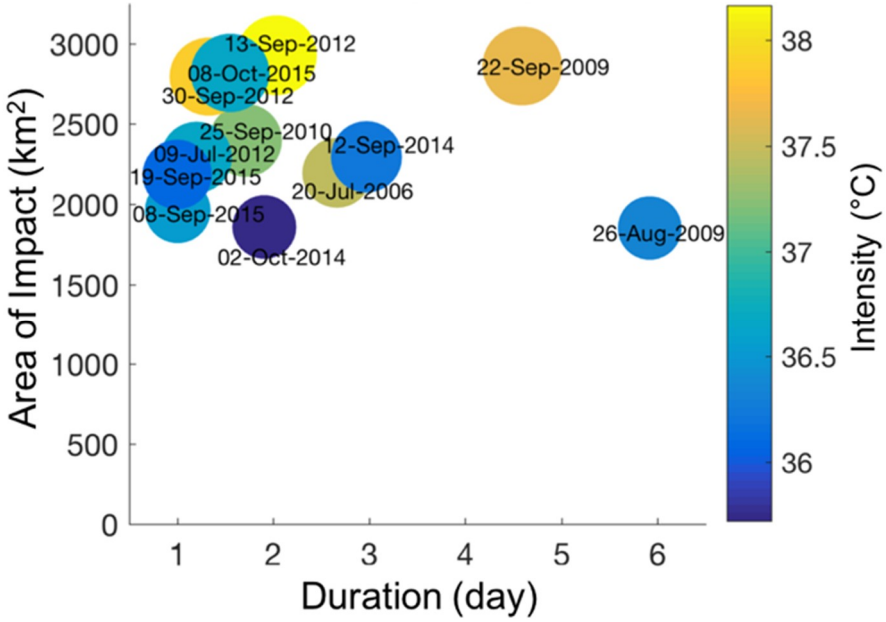

Figure 2. High-impact heat waves occurring in Los Angeles County during the historical period of 2001–2015: correspondence between heat waves' area of impact, duration, and intensity (average daily maximum air temperature during the heat wave).

2.4. Urban Morphology Information

To simulate and generate heat emission profiles of urban buildings in LA, it was first necessary to develop a city-scale dataset of the existing building stock, including geometries and building characteristics. The building geometry information usually includes the footprint and height, while the building characteristics include the year built, number of stories, and use type of each building [47]. We collected the related city building datasets using a geographic information system (GIS) approach. The 3D city geometries, including building outlines and height information, were collected from the Los Angeles Region Imagery Acquisition Consortium (LARIAC) program. The program provides digital aerial imagery data with the collaborative participation of LA County departments, municipal governments, and many other public agencies [48]. The geodatabase in shapefile format with attributes, delivered as a product of LARIAC 4 in 2014, was used in this study. Other building attributes, including the number of floors and building land use codes, were collected from the assessor parcels data in 2017 from the city's open data portal [49]. The geodatabase was transformed into the GeoJSON format, and the parcel property information of each building was mapped accordingly.

Overall, a total of 1,108,673 buildings were collected from the LARIAC4 product, located across 1071 census tract districts in the city of LA. As a validation, we first calculated the building footprint area and removed those with a footprint area less than 30 m^2, which is considered too small for building representations. We then mapped the land use code to clusters of building types, including Single Family Home, Multifamily, Office, Retail, School, Hospital, Hotel, Restaurant, and Others (warehouse, facility, vacant, and miscellaneous). Among the rest of the 951,680 valid buildings, 99.3% had a valid building use type in one of these. To calculate the total floor area of the buildings, we used the building height information to cross-validate the floor numbers by examining the height per floor, assuming floor height was within the range of 2.6 m to 6 m. Altogether, 97.4% had a valid floor height, and we corrected the rest by back-calculating the floor numbers using the total height divided by an average floor height of 3 m. The final floor areas were calculated based on the footprint area multiplied by the corrected number of floors. Figure 3 shows the square footage distribution of the buildings (only buildings under 3000 square foot are showed). Overall, 50% of the buildings are less than 213 m^2, and 99% are less than 5671 m^2.

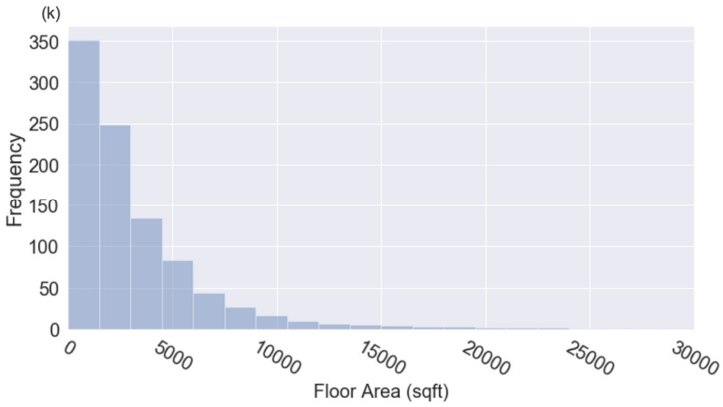

Figure 3. Floor area distribution of all buildings in the city of LA.

Based on the building use type and square footage, we further categorized the buildings into 13 prototypes, as listed in Figure 4. In LA city, more than 94% of the buildings are residential, represented by the LSF (large single-family home), SSF (small single-family home), and MF (multifamily).

Across the city, the buildings have a heterogeneous spatial distribution. Figure 5 plots the census tract level building density ratio, calculated by aggregating the district level total building floor area and divided by the district total/footprint area. In general, the buildings are densely distributed in the commercial areas of the Downtown, Hollywood, and Westwood neighborhoods, as well as the

residential areas in north Hollywood neighborhoods. The local buildings waste heat dispersions were determined by the urban morphology, including urban building densities and land use types.

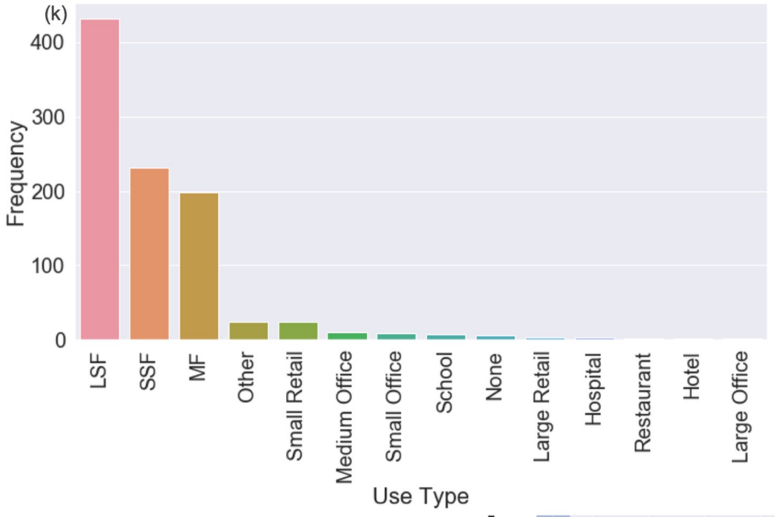

Figure 4. Building type distribution of all buildings in the city of LA.

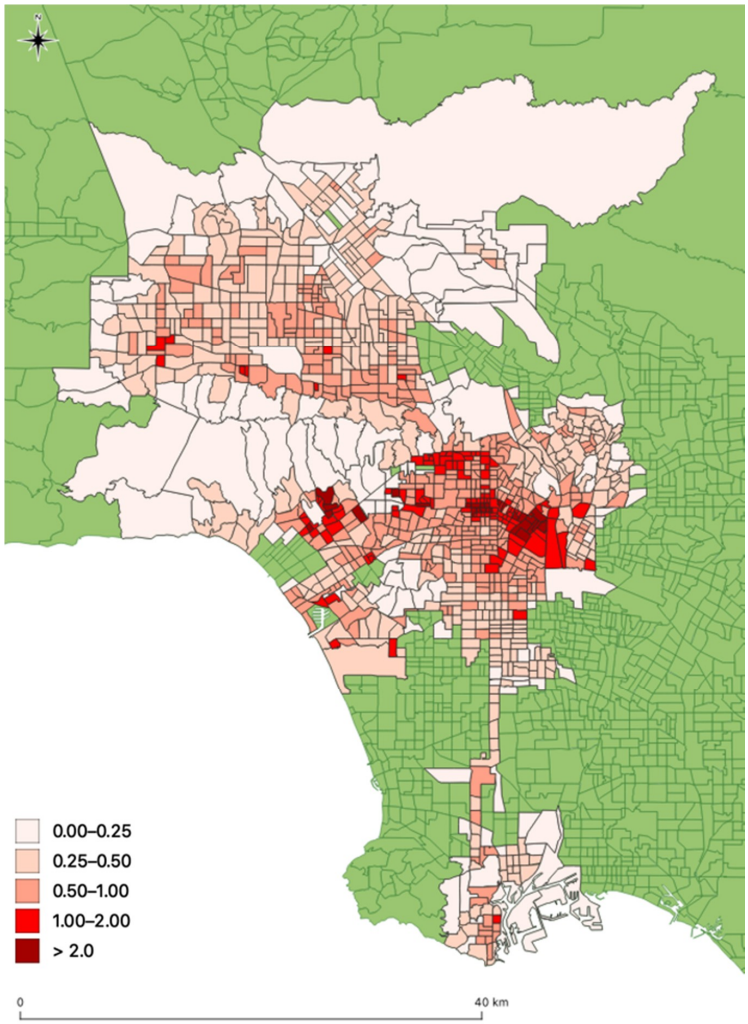

Figure 5. Census tract building density ratio in the city of LA.

2.5. Building Waste Heat Simulation with EnergyPlus

EnergyPlus [50] is the U.S. Department of Energy's flagship building energy software for simulating the dynamic energy and environmental performance of buildings. An EnergyPlus model calculates a building's thermal loads, system response to those loads, and resulting energy use, along with related metrics like occupant comfort and energy costs. Since the EnergyPlus version 9.1.0 release, a bottom-up approach is incorporated in the program to simulate and report the run-time calculated building heat emission at the thermal zone and building levels [14]. In EnergyPlus, heat emissions are calculated, aggregating heat generated from envelopes, zones, and HVAC systems. The heat released by the building envelope component includes the radiative and convective heat transfer to outdoor air due to the temperature difference between the surface temperature and the outdoor air dry-bulb temperature. The zone component includes air discharged from exfiltration through openings (e.g., windows, doors) and cracks, and from the air release from exhaust fans through mechanical ventilation. The heat released by the HVAC systems includes the relief air from the air handling units (AHU) and fuel combustion discharge, as well as the heat rejected zone and system HVAC components. The model employs physics-based heat balance equations, and can be used with any weather dataset and any building topology. The results can be reported with spatial and temporal flexibility. In this study, we applied this feature of EnergyPlus to generate building-level heat emission profiles under heat wave events.

As introduced, EnergyPlus calculates and reports building heat emissions from: convective and radiative heat emissions from the envelope to the ambient air, and exhaust and relief heat through exfiltration and the system with moist air. It also calculates and reports building heat emissions from sensible and latent heat rejection through (1) air-cooled, evaporative-cooled, and water-cooled condensing units of cooling coils, heating coils, and water heaters; zone HVAC forced air units; evaporative coolers; and more, and (2) plant condensing equipment such as water-cooled chillers. As WRF has already considered the surface solar radiation budget in its heat balance calculations, here we only report the waste heat generated through air exchange with the atmosphere and through HVAC system rejection.

Thirteen prototype EnergyPlus models were chosen to cluster all buildings in the city; namely, small single-family (SSF), large single-family (LSF), multi-family (MF), large office, medium office, small office, large retail, small retail, school, hospital, hotel, restaurant, and warehouse. Among them, the three residential types were generated assuming they complied with the California Title 24 Building Energy Efficiency Standards for the LA climate zone. The commercial types were collected from ASHRAE prototype building models based on ASHRAE Standard 90.1-2010 for the climate zone of southern California. These models were developed by Pacific Northwest National Laboratory in support of the U.S. Department of Energy's Building Energy Codes Program [51].

To consider the spatial and temporal variabilities of AH from buildings under the studied heat wave, we derived hourly weather data files in EnergyPlus Weather (EPW) file format for each grid (500 m $\times$ 500 m) from the 15-day WRF-UCM simulation results from 14 to 28 September 2009. Specifically, hourly barometric pressure, dry bulb temperature, relative and specific humidity, wind speed, wind direction, direct and diffuse downwelling short wave solar radiation were extracted from WRF outputs to overwrite the EPW files. Prototype simulations were performed at the grid level to generate heat emission profiles (hourly heat flux per building floor area) based on grid level urban use types and distributions. For example, if SSF, LSF, and MF buildings were presented in one WRF grid, the prototypes simulations were performed accordingly with the 15-day weather data for this grid. For an individual building in the LA building dataset, the AH profile was then calculated with its corresponding prototype heat flux intensity multiplied by its total floor area, according to the building's use type and grid location.

2.6. Urban Building Heat Emission Profiles

Before aggregating the building level heat emission profile to grids, we first collected energy measurement data to verify our assumptions on the representativeness of building prototypes and their spatial distributions across the city. Although the energy specifics of individual buildings cannot be precisely modeled or measured, the magnitude and distributions of the energy use intensity (EUI) of a group of buildings should statistically match with the measured ground truth. To achieve this, we acquired the measured EUI of each census tract in LA city from the Energy Atlas database. The Energy Atlas is a database of building energy consumption that links utility account information to building characteristics that can be expressed spatially. Annual EUI was extracted from 751 census tracts that have valid data for 2016. We then conducted an annual simulation of the prototype models using the 2016 historical weather data at LAX airport, and gathered the total floor area and energy use for each census tract area to deduce the simulated EUI. Figure 6 visualized the distributions of the measured and simulated EUI profile, namely EUI-ATLAS and EUI-LARIAC. On the whole, the average measured and estimated annual EUI were 81.9 kilowatt-hours per square meter (kWh/m^2) and 87.8 kWh/m^2, respectively. For each census tract area, the estimated EUI values (EUI-LARIAC) had a strong positive correlation with the measured values (EUI-ATLAS), with an R-squared value of 0.646, indicating the prototype aggregations performed a reasonable prediction of the district energy use performance. The estimations had a relatively centered distribution, as the prototype EUIs were pre-assumed and had less variation than the real scenarios.

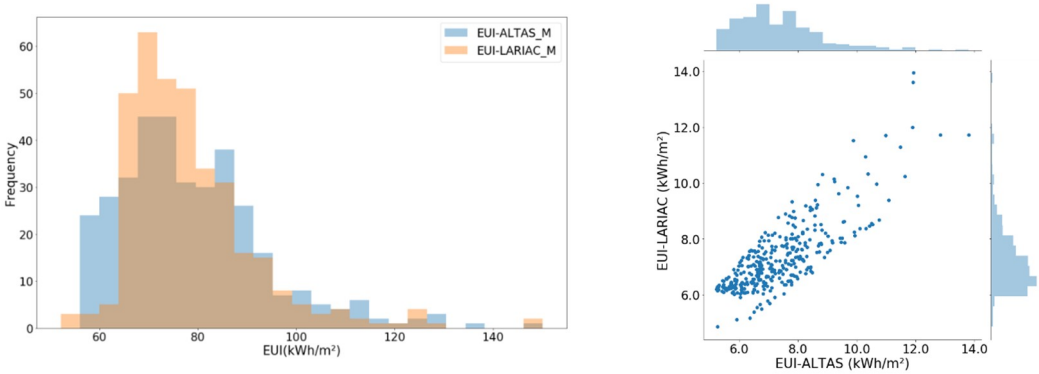

(**a**) Histogram of distributions (**b**) Joint plot of distributions

Figure 6. Distributions of the measured and simulated census tracts average EUI (kWh/m^2). (**a**): Histogram of distributions, (**b**): Joint plot of distributions.

Figure 7 further demonstrates that the estimated EUI had a similar spatial distribution to that of the Energy Atlas measured EUI, particularly in dense urban areas with an average EUI of more than 100 kWh/m^2, such as Downtown and Hollywood. Nonetheless, the residential area in South LA was overestimated, while that in the South Valley was underestimated, due to the simplification in the modeling and simulation processes.

For assumptions of the spatial distributions of the building models and their energy properties, we used the bottom-up approach to gather the grid-level heat emission intensity profiles. Explicitly, the hourly AH flux from buildings (Q_A) was calculated as:

$$Q_A = \frac{\sum_1^n Q_p A_i}{\sum_1^n A_i}, \quad (1)$$

where n is the total number of buildings in each grid, Q_p is the prototype heat emission flux in watts per square meter based on the building's type and grid ID, and A_i is the floor area of the building.

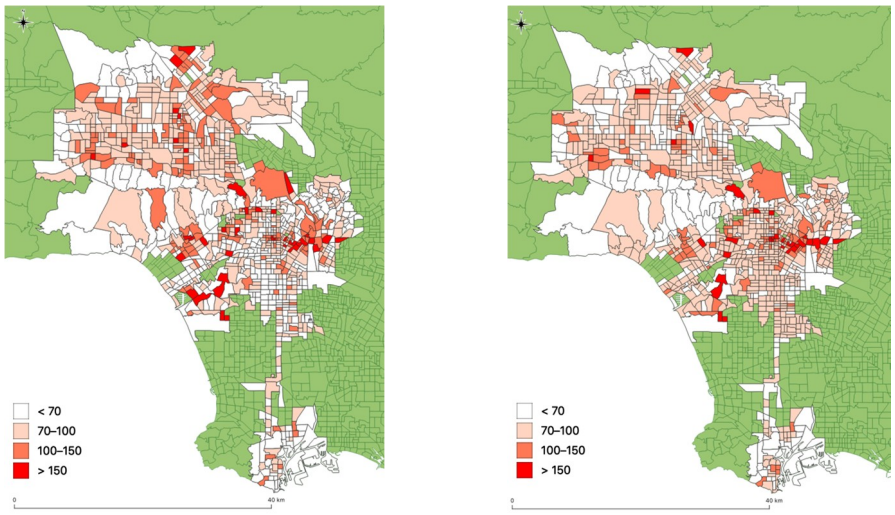

(**a**) EUI-ALTAS (kWh/m²) (**b**) EUI-LARIAC (kWh/m²)

Figure 7. Census tracts building annual EUI distribution. (**a**): EUI-ALTAS (kWh/m^2), (**b**) EUI-LARIAC (kWh/m^2).

3. Results

3.1. The Heat Wave and Its Energy Impact

Extreme heat events can influence building performance and waste heat discharge in several ways. For example, higher dry-bulb temperature and stronger solar radiation can increase the cooling loads, while relative humidity affects the building's latent load. Examining the patterns of change in the different metrological variables exported from WRF, the dry-bulb temperature, relative humidity, and wind speed had the most significant and representative amount of variation from regular summer weather during the five-day heat wave period.

Figure 8a plots the grid average dry-bulb temperature, as the most explicit indicator of the heat wave, for the 15-day WRF simulation period from 14 September (Day 0) to 28 September (Day 15). The figure indicates that the heat wave started on 22 September (Day 8) and ended on 27 September (Day 13). For illustration, we designated the five days from 22 September to 27 September as the heat wave days, and in comparison, another five days one week ahead (from 15 September to 20 September) as the non-heat wave days, representing typical non-extreme summer weather. Overall, the hourly average air temperature of all grids during the heat wave days was 29.8 °C, while the average of non-heat wave days was 22.5 °C. The peak temperatures during the heat wave and non-heat wave days were 37.5 °C and 33.5 °C, averaging all grids. Figure 8b plots the spatial distribution of the temperature at 2:00 pm on selected days. During the heat wave days, the temperatures had a more notable coast-to-inland difference, while the inland local air temperature reached as high as above 45 °C.

A significant decrease in relative humidity also was observed during the heat wave days (Figure 9). The average relative humidity during the non-heat wave days was 57.6%, while during the heat wave period it was as low as 18.3%. However, the coastal areas were less influenced by the heat wave. The outdoor humidity influenced the latent cooling loads of the buildings and the latent heat removed from the buildings by the air-conditioning.

Outdoor wind speed affects the air pressure distribution on building surfaces and impacts the amount of infiltration and exfiltration and convective heat transfer from surface to ambient air. The air circulation around buildings strongly affects the effectiveness of air-conditioning efficiencies, such as cooling towers. Figure 10 shows the temporal and spatial variations of the wind speed. At the beginning of the heat wave days, the wind is notably stronger than it is on the non-heat wave days, yet the strong gusts mostly took place in the non-urban valley areas, and the city area was not affected.

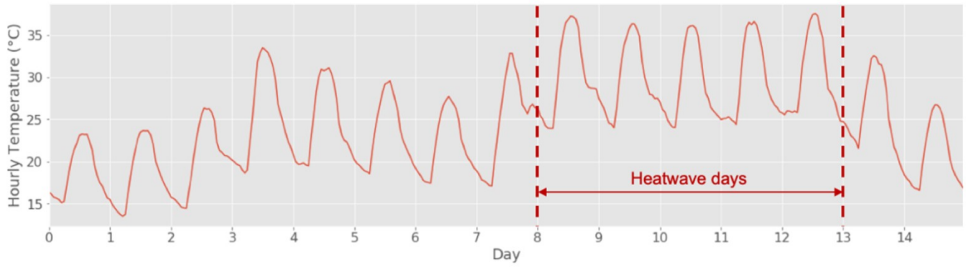

(**a**) Temporal variation (averaged over all grids)

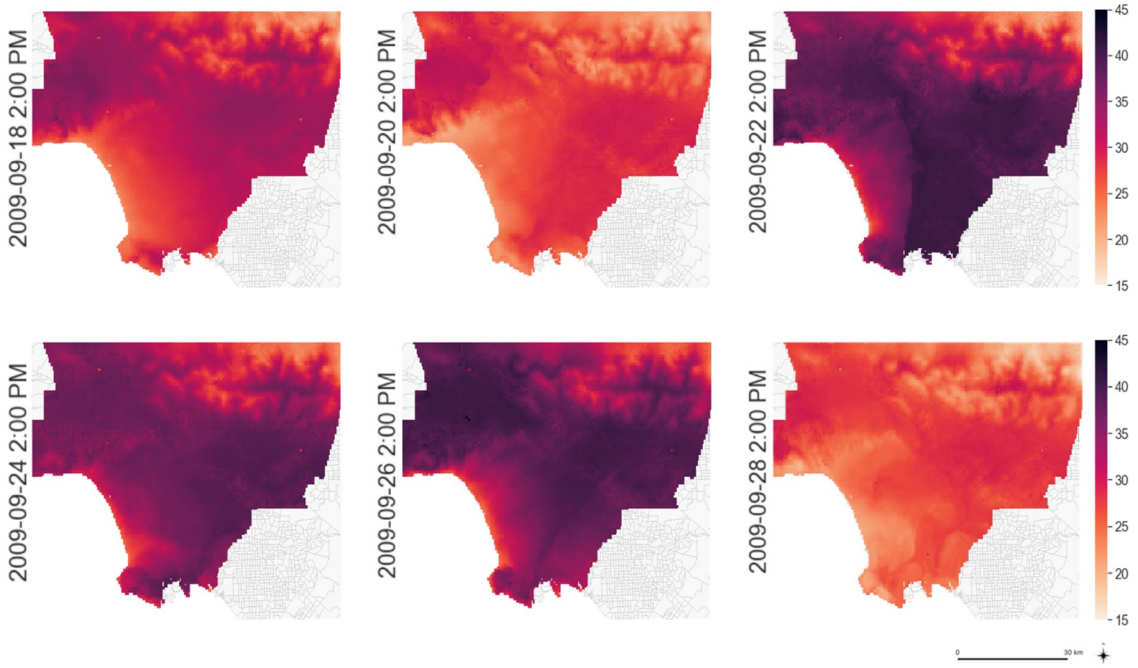

(**b**) Spatial distribution

Figure 8. Dry-bulb temperature (°C) distribution during the heat wave. (**a**): Temporal variation (averaged over all grids), (**b**) Spatial distribution.

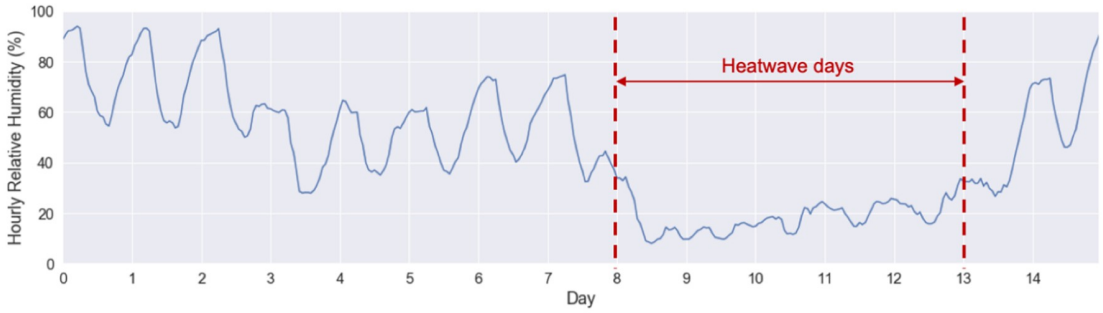

(**a**) Temporal variation (averaged over all grids)

Figure 9. *Cont.*

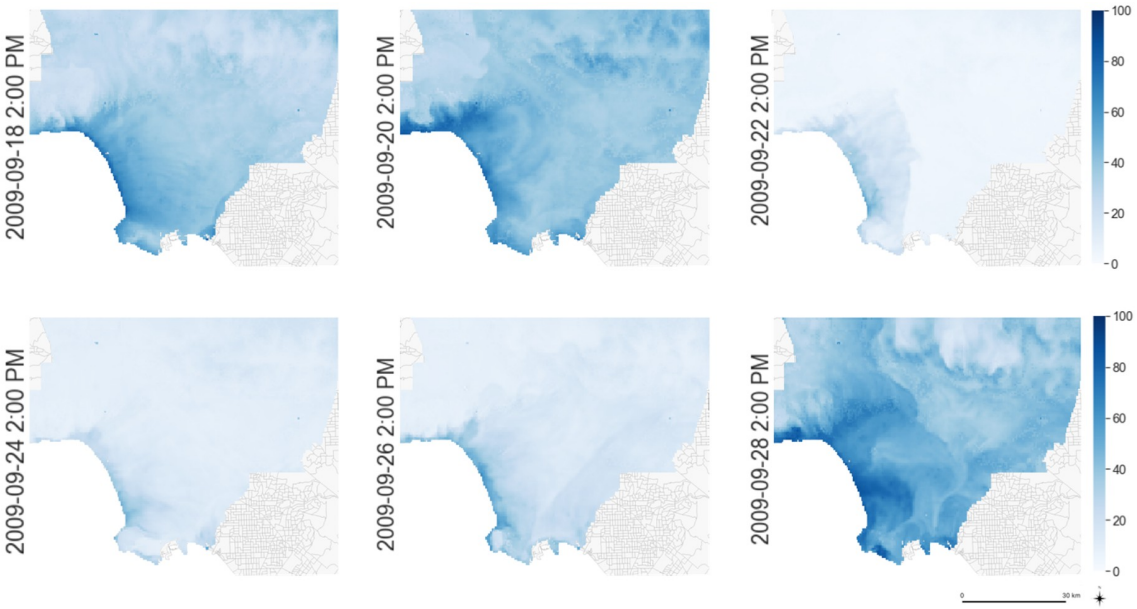

(**b**) Spatial distribution

Figure 9. Relative humidity (%) distribution during the heat wave. (**a**): Temporal variation (averaged over all grids), (**b**) Spatial distribution.

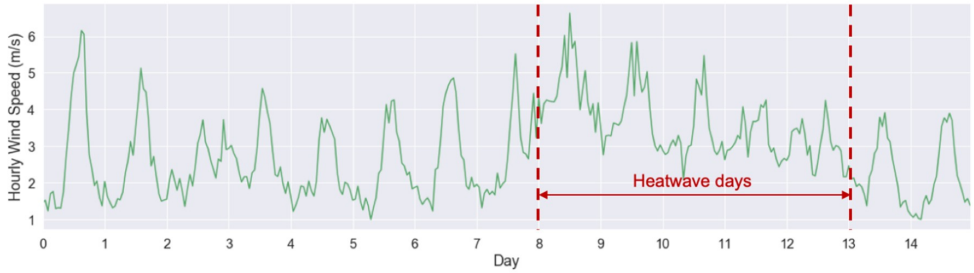

(**a**) Temporal variation (averaged over all grids)

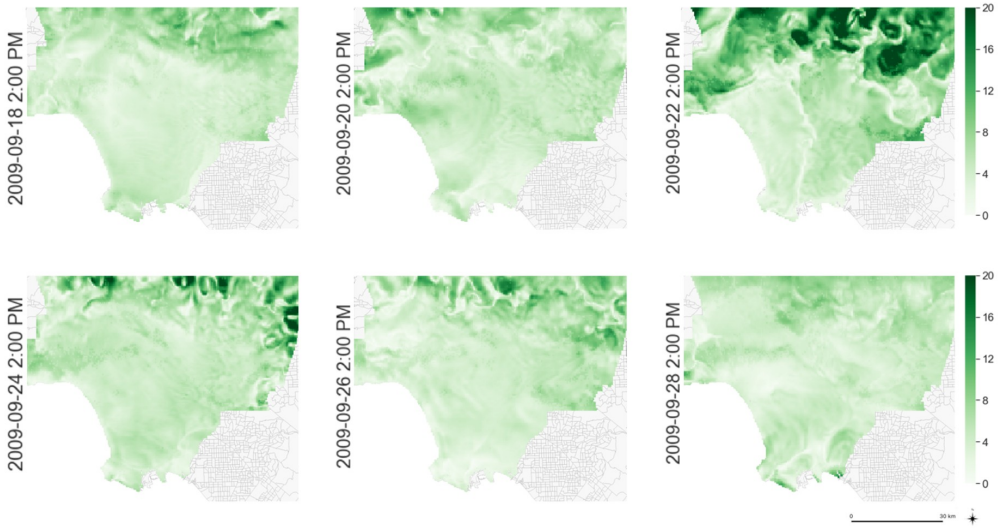

(**b**) Spatial distribution

Figure 10. Wind speed (m/s) distribution during the heat wave. (**a**): Temporal variation (averaged over all grids), (**b**) Spatial distribution.

3.2. Temporal Variations of Anthropogenic Heat Intensity

The heat emission results are aggregated to grid level in hourly heat flux profiles, normalized by the grid's total building footprint area. Figure 11 presents the grid-average curve throughout the 15 simulation days. The grid-average and grid-medium heat flux were 30.9 watts per square meter (W/m^2) and 25.2 W/m^2, which were 19.9% and 10.6% greater than the non-heat wave days one week ahead. The highest grid-average heat discharge occurred on 24 September, at 3:00 pm, when it reached 60.8 W/m^2. In comparison, the peak energy demand during the heat wave days was on average 24% greater than the non-heat wave days. And the peak temperature during the heat event mostly appeared at about 12:00 pm, while the peak heat emission mostly appeared at 3–4 pm. The three-hour delay in peak AH was mainly due to the thermal lag in heat transfer between the outdoors and indoors due to the building's thermal mass.

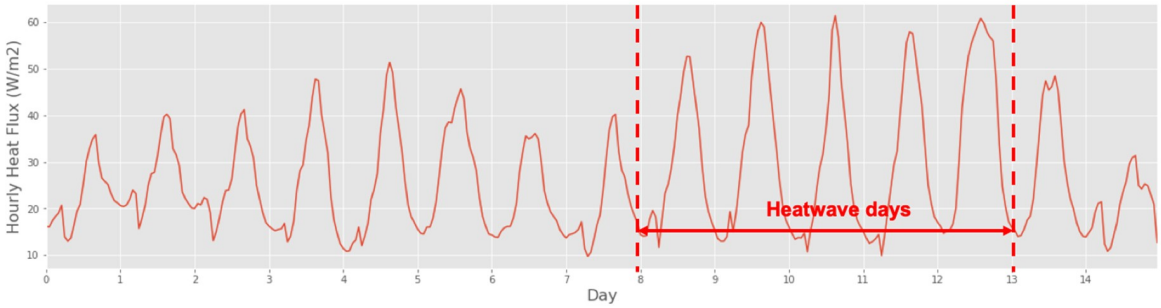

Figure 11. Grid-average hourly heat flux from buildings to the atmosphere.

Figure 12 plots the average diurnal hourly AH profiles of the heat wave and non-heat wave days. The heat flux differences increased when the temperature differences increased during the day time, and peaked around 4 pm when the mean heat flux of heat-wave days reached 56.2 W/m^2, which was 30.8% greater than the non-heat wave day average.

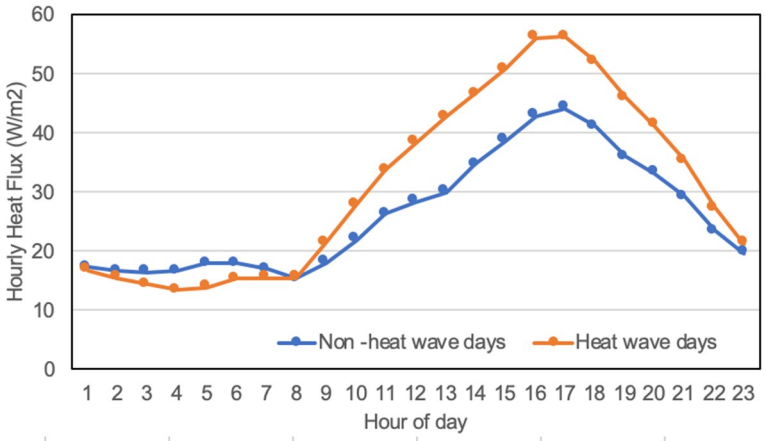

Figure 12. Diurnal profile of the hourly AH flux during non-heatwave and heat wave days.

Figure 13 plots the relationship between the heat flux discharged from buildings and the outdoor air temperature during the daytime of the simulation period. Overall, the trend is linear. The hourly heat flux increased by 1.72 W/m^2, with a 1 °C increase in the outdoor air temperature.

Figure 14 plots the hourly AH heat flux from the building waste heat by the source components, including air exfiltration and fan exhaust (EXH), relief air through mechanical systems (REL), and heat rejection from air-conditioning (REJ). Throughout the studied period, the AC heat rejection made the most contribution (86.5%) to the AH dispersion. During the heat wave days, due to the higher

cooling load of the AC systems, the average REJ was 77% more than it was on the non-heat wave days (33.6 W/m^2 compared to 19.0 W/m^2). The AH from the EXH and REL were negative, offsetting the total heat discharge, as the outdoor air was hotter than the indoor air or system relief air from the buildings. During the nighttime, the HVAC systems of most commercial buildings are mostly off, and the heat rejection is much lower. Because of the thermal lag, the buildings release cooled indoor air to the outdoors at night, instead of dispersing heat to the environment. The total heat emission during the daytime between sunrise and sunset time (6:00 am to 7:00 pm) was about 2.3 times that of the heat emission during the night.

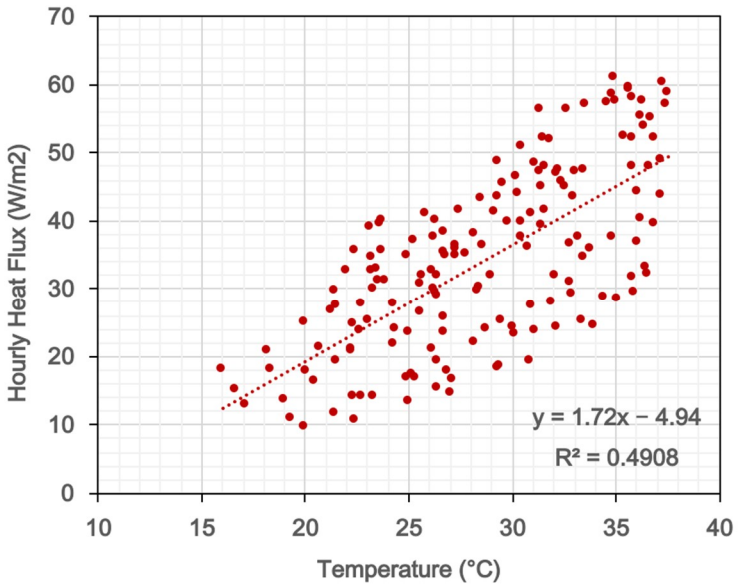

Figure 13. Heat flux versus outdoor air temperature.

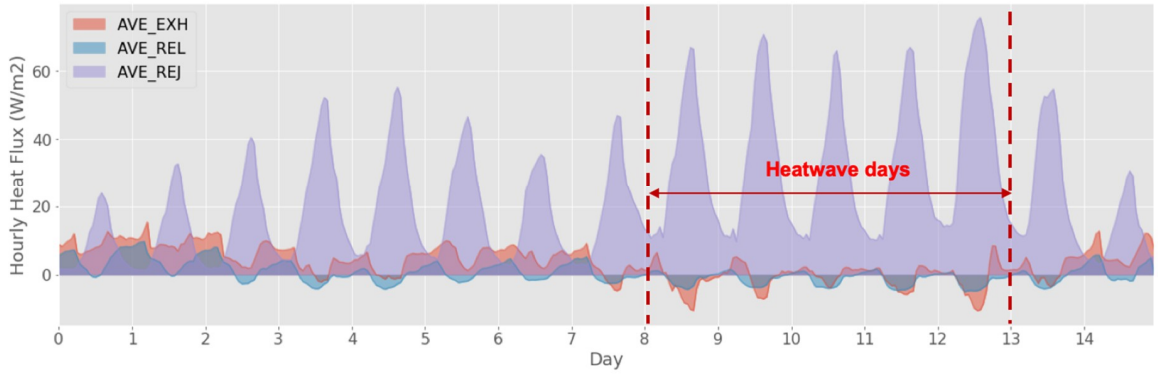

Figure 14. Component level of the hourly heat flux of the building waste heat.

Figure 15 presents the heat flux curve for residential and commercial buildings separately. Although 94.3% of the buildings in LA city are the residential type, they are only 60.5% of the total building floor area. During the heat wave days, the residential buildings contributed to 52.5% of the total waste heat discharge. Also, the heat emission from residential buildings and commercial buildings peaked at different times of the day. Commercial buildings mostly have daytime working schedules and usually a daily emission curve that peaks at noontime, while the residential sector peak occurs during the late afternoon, about 4 pm to 6 pm. The overall daily peak showed at 3 pm each day during the five-day heat event.

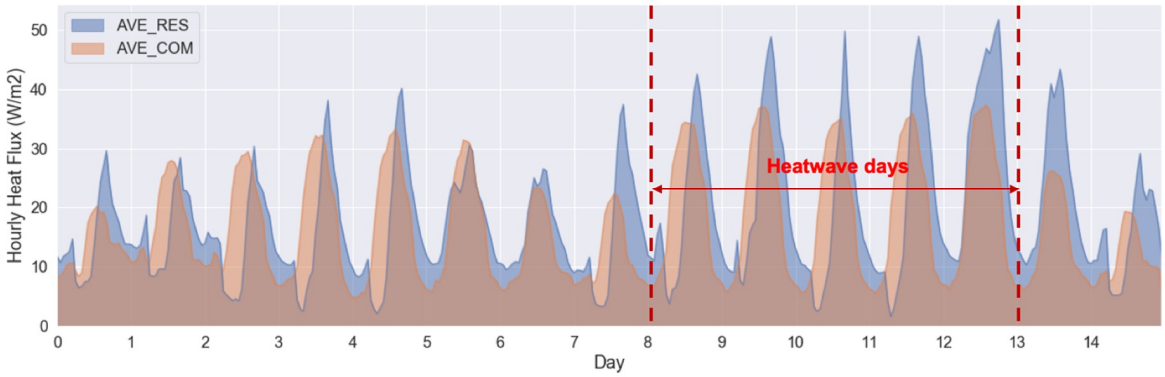

Figure 15. Hourly heat flux from the residential and commercial sectors.

3.3. Spatial Variations of Anthropogenic Heat Intensity

The spatial variations of the AH intensities from the buildings in the study are show in Figure 16. The hourly bars in Figure 16a represent the spatial ranges (without outliers) over all grids in the simulation domain, while the boxes represent the 75th and 25th percentiles. Heat maps represented in Figure 16b indicate that in the central downtown area of LA, the grid-level heat flux could reach above 200 W/m^2 while the grid-average at the same hour was only about 50 W/m^2. Generally, the ranges of the heat flux at each hour are large, and the distributions are uneven.

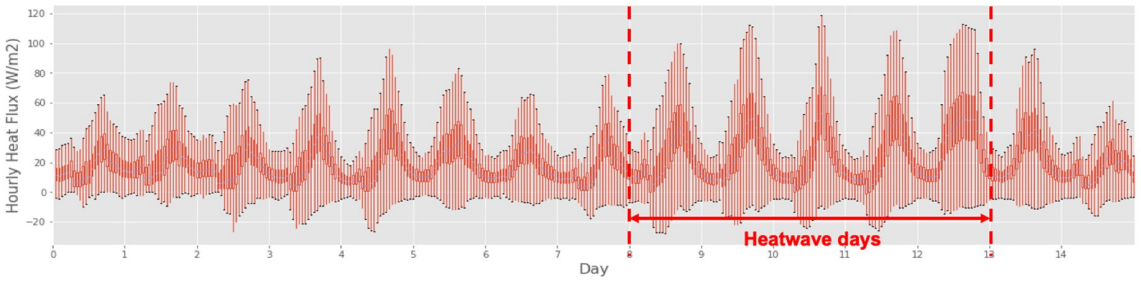

(**a**) Box plot

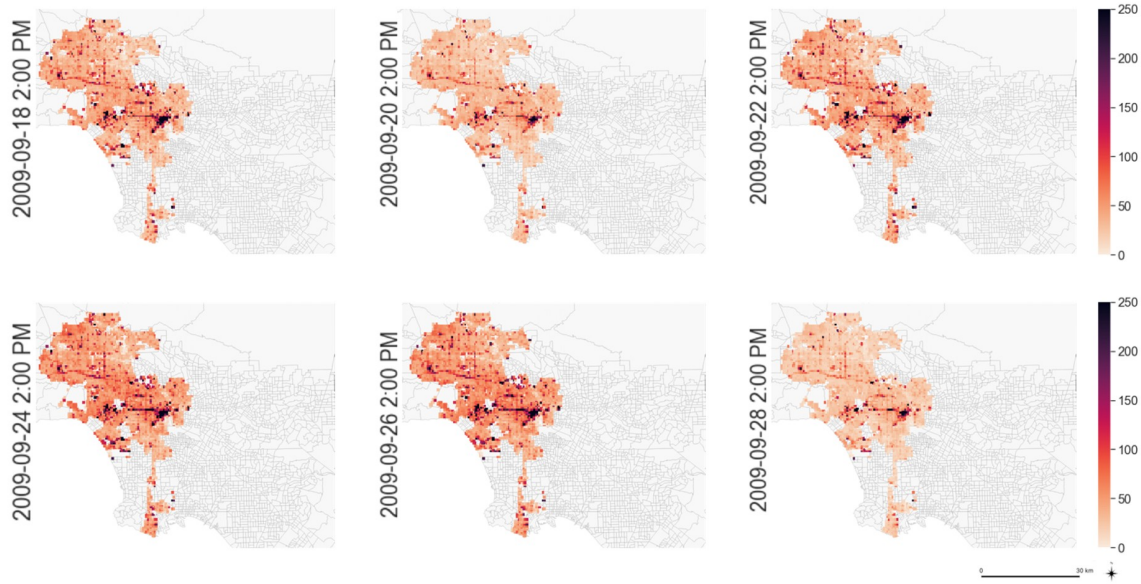

(**b**) Heatmap

Figure 16. Spatial distributions of the heat flux from buildings. (**a**): Box plot (**b**): Heatmap.

The spatial variation results from both microclimate variability (coastal versus inland areas) and urban morphology variability (downtown versus residential areas) in determining the waste heat per floor area of buildings or footprint under extreme heat conditions. To understand how each factor contributes to the major discrepancy in the spatial distributions of AH, we analyzed the heat emission intensity per building floor area for the LSF as an example prototype. Figure 17 plots the 95th and 5th percentiles of the hourly heat flux intensity of LSF under the range of grid-level microclimate conditions without taking the grid level urban footprint into account. Under the spatial variations of outdoor air conditions, the emission intensity varied accordingly, and showed a wider range during hotter days. On 24 September, with the hottest weather, the 5th percentile of the AH intensity of all grids was 26.2 W/m^2, and the 95th percentile was up to 34.6 W/m^2.

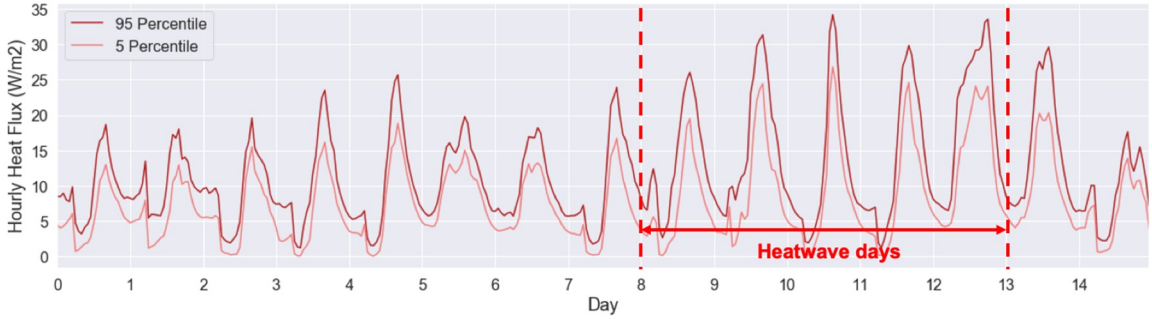

Figure 17. Percentiles of the heat emission intensities: large single-family houses.

Figure 18 further plots the spatial variations of the heat emission intensities of LSF under county-wide microclimate simulated by WRF at the hottest hour on the hottest day (24 September, 2 pm) during the heat wave event. The AH intensity values of the inland area reached 35 W/m^2, comparing to the values of the coastal area at around 25 W/m^2. Overall, although the urban morphology plays a major role in AH spatial variation, the variances caused by microclimate cannot be ignored.

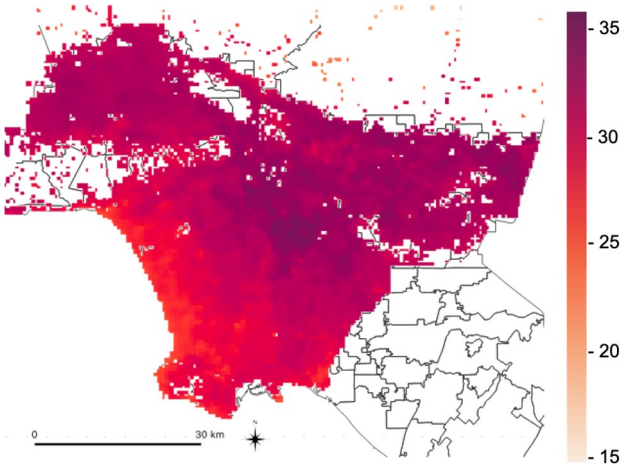

Figure 18. Heat emission intensities of large single-family houses under county-wide microclimate.

4. Discussion

Quantifying the event-specific buildings waste heat discharge, using physics-based building modeling and spatially resolved urban microclimate information, could help advance our understanding of the response of urban microclimate to anthropogenic heating under extreme weather events. With bottom-up calculations of heat emission from different building system components, and aggregations of building-level hourly discharge to urban grid-level, temporal and spatial variations

in urban land-use were taken into consideration, including the differences in peak time and amount of the commercial or residential building types. The results from these simulations indicated a potential that the increased use of air-conditioning during the heat waves would exacerbate the waste heat discharge to the local atmosphere, and consequently lift the urban air and surface temperatures, which in turn increase the air-conditioning loads in buildings. The WRF-UCM modeling system used in this study relied on a predetermined and fixed diurnal anthropogenic heat profile to represent building heat emissions feedback to the urban environment, as an extra sensible heat flux term which was added to the surface energy balance over urban grid cells [31,32]. Replacing this default parameterization with the domain-specific, event-specific representation of anthropogenic heating, produced in this study, enhanced the model's performance in capturing urban microclimate dynamics, and in turn, our understanding of the interactions between urban microclimate and building heat emissions, particularly under extreme heat conditions and a changing climate.

It should be noted that the hourly profiles developed here relied on assumptions that could limit their accuracy and general applicability. First, the individual building emission intensities were based on prototype models, which are less flexible for representing the complexity of real urban building topologies. In particular, the year of build and renovation history were not included in further diversifying the prototypes. These factors also determined the building envelope configurations and the system efficiencies of the buildings, and may consequently influence the aggregated AH flux results. Second, the urban morphology data acquired from open data sources may lack accuracy, as the geometry data were extracted with simplifications from imagery, and the parcel data were acquired manually and updated during the years of investigation. Further refinements of such assumptions, regarding higher fidelity of the data and models applied in the simulation, may be required in order to apply the method to other cities and regions.

5. Conclusions

A bottom-up building heat emission model with urban building energy modeling was developed to investigate the temporal and spatial variations of waste heat fluxes in the entire city of LA under an extreme heat event in September 2009. The results indicate the average AH discharges from buildings can increase by up to 20% on average during a heat wave compared to the regular summer weather. The spatial distribution of heat fluxes is mostly influenced by the city's urban morphology, including urban building density and variations in residential and commercial building distributions. The impact of microclimate variation is also notable, considering the coast-to-inland temperature and humidity differences.

The bottom-up simulation approach provided a high-resolution representation of the magnitude and distributions of the buildings' AH profiles under extreme heat. The approach adopting physical models is flexible enough to be applied to any weather conditions with any urban forms, and the results can be aggregated at any certain scales, from pixel grid to a whole city region. The results serve as a fundamental step toward a continued investigation of the feedback of AH fluxes to urban climate and microclimate simulations of extreme weather events. The increase in AH generated and discharged during heat waves may in turn exacerbate hot weather locally. It is necessary to combine high-resolution microclimate simulation with high-resolution building heat emission simulation and investigate the two-way data exchange to consider the dynamic interactions between both models. Such an investigation will improve evaluations of strategies to mitigate urban overheating during heat waves.

Author Contributions: Conceptualization, X.L., P.V., T.H. and A.J.; methodology, X.L. and P.V.; software, X.L. and P.V.; validation, X.L.; formal analysis, X.L.; investigation, X.L.; resources, X.L. and P.V.; data curation, X.L. and P.V.; writing—original draft preparation, X.L. and P.V.; writing—review and editing, T.H. and A.J.; visualization, X.L. and P.V.; supervision, T.H. and A.J.; project administration, A.J.; funding acquisition, A.J. All authors have read and agreed to the published version of the manuscript.

Funding: This research was supported by the U.S. Department of Energy, Office of Science, as part of research in the MultiSector Dynamics, Earth and Environmental System Modeling Program.

Acknowledgments: Authors thank Stephanie Pincetl of University of California, Los Angeles and LADWP (The Los Angeles Department of Water and Power) for providing the annual building energy use data aggregated at the census tract level. This research used resources of the National Energy Research Scientific Computing Center (NERSC), a DOE Office of Science User Facility supported by the Office of Science of the US Department of Energy under Contract No. DEAC02-05CH11231.

Conflicts of Interest: The authors declare no conflict of interest.

References

1. NOAA National Centers for Environmental Information. Global Climate Report—July 2019, (n.d.). Available online: https://www.ncdc.noaa.gov/sotc/global/201907 (accessed on 2 August 2020).
2. July 2019 was Hottest Month on Record for the Planet|National Oceanic and Atmospheric Administration, (n.d.). Available online: https://www.noaa.gov/news/july-2019-was-hottest-month-on-record-for-planet (accessed on 3 August 2020).
3. Sun, K.; Specian, M.; Hong, T. Nexus of thermal resilience and energy efficiency in buildings: A case study of a nursing home. *Build. Environ.* **2020**, *177*, 106842. [CrossRef]
4. Li, D.; Bou-Zeid, E. Synergistic Interactions between Urban Heat Islands and Heat Waves: The Impact in Cities Is Larger than the Sum of Its Parts. *J. Appl. Meteorol. Clim.* **2013**, *52*, 2051–2064. [CrossRef]
5. Lemonsu, A.; Viguie, V.; Daniel, M.; Masson, V. Vulnerability to heat waves: Impact of urban expansion scenarios on urban heat island and heat stress in Paris (France). *Urban Clim.* **2015**, *14*, 586–605. [CrossRef]
6. Ren, G.-Y. Urbanization as a major driver of urban climate change. *Adv. Clim. Chang. Res.* **2015**, *6*, 1–6. [CrossRef]
7. IPCC. *Painel Intergovernamental sobre Mudanças Climáticas, Climate Change 2014: Mitigation of Climate Change*; Contribution of Working Group III to the Fifth Assessment Report of the Intergovernmental Panel on Climate Change; Cambridge University Press: Cambridge, UK, 2014. [CrossRef]
8. Creutzig, F.; Baiocchi, G.; Bierkandt, R.; Pichler, P.-P.; Seto, K.C. Global typology of urban energy use and potentials for an urbanization mitigation wedge. *Proc. Natl. Acad. Sci. USA* **2015**, *112*, 6283–6288. [CrossRef]
9. Wu, X.; Wang, L.; Yao, R.; Luo, M.; Wang, S.; Wang, L. Quantitatively evaluating the effect of urbanization on heat waves in China. *Sci. Total. Environ.* **2020**, *731*, 138857. [CrossRef]
10. Sailor, D.J.; Georgescu, M.; Milne, J.M.; Hart, M.A. Development of a national anthropogenic heating database with an extrapolation for international cities. *Atmospheric Environ.* **2015**, *118*, 7–18. [CrossRef]
11. Vogel, M.M.; Zscheischler, J.; Wartenburger, R.; Dee, D.; Seneviratne, S.I. Concurrent 2018 Hot Extremes Across Northern Hemisphere Due to Human-Induced Climate Change. *Earth's Future* **2019**, *7*, 692–703. [CrossRef]
12. Sailor, D.; Vasireddy, C. Correcting aggregate energy consumption data to account for variability in local weather. *Environ. Model. Softw.* **2006**, *21*, 733–738. [CrossRef]
13. Sun, R.; Wang, Y.; Chen, L. A distributed model for quantifying temporal-spatial patterns of anthropogenic heat based on energy consumption. *J. Clean. Prod.* **2018**, *170*, 601–609. [CrossRef]
14. Hong, T.; Ferrando, M.; Luo, X.; Causone, F. Modeling and analysis of heat emissions from buildings to ambient air. *Appl. Energy* **2020**, *277*, 115566. [CrossRef]
15. Sailor, D.J.; Lu, L. A top–down methodology for developing diurnal and seasonal anthropogenic heating profiles for urban areas. *Atmos. Environ.* **2004**, *38*, 2737–2748. [CrossRef]
16. Ching, J.; Brown, M.J.; McPherson, T.; Burian, S.; Chen, F.; Cionco, R.; Hanna, A.; Hultgren, T.; Sailor, D.; Taha, H.; et al. National Urban Database and Access Portal Tool. *Bull. Am. Meteorol. Soc.* **2009**, *90*, 1157–1168. [CrossRef]
17. Nie, W.; Zaitchik, B.F.; Ni, G.; Sun, T. Impacts of Anthropogenic Heat on Summertime Rainfall in Beijing. *J. Hydrometeorol.* **2017**, *18*, 693–712. [CrossRef]
18. Bohnenstengel, S.I.; Hamilton, I.; Davies, M.; Belcher, S.E. Impact of anthropogenic heat emissions on London's temperatures. *Q. J. R. Meteorol. Soc.* **2013**, *140*, 687–698. [CrossRef]
19. Ohashi, Y.; Genchi, Y.; Kondo, H.; Kikegawa, Y.; Yoshikado, H.; Hirano, Y. Influence of Air-Conditioning Waste Heat on Air Temperature in Tokyo during Summer: Numerical Experiments Using an Urban Canopy Model Coupled with a Building Energy Model. *J. Appl. Meteorol. Clim.* **2007**, *46*, 66–81. [CrossRef]

20. Ichinose, T.; Shimodozono, K.; Hanaki, K. Impact of anthropogenic heat on urban climate in Tokyo. *Atmos. Environ.* **1999**, *33*, 3897–3909. [CrossRef]
21. Bueno, B.; Norford, L.; Pigeon, G.; Britter, R. A resistance-capacitance network model for the analysis of the interactions between the energy performance of buildings and the urban climate. *Build. Environ.* **2012**, *54*, 116–125. [CrossRef]
22. A Benz, S.; Bayer, P.; Menberg, K.; Jung, S.; Blum, P. Spatial resolution of anthropogenic heat fluxes into urban aquifers. *Sci. Total. Environ.* **2015**, *524–525*, 427–439. [CrossRef]
23. Feng, J.-M.; Wang, Y.-L.; Ma, Z.-G.; Liu, Y. Simulating the Regional Impacts of Urbanization and Anthropogenic Heat Release on Climate across China. *J. Clim.* **2012**, *25*, 7187–7203. [CrossRef]
24. Lindberg, F.; Grimmond, C.; Yogeswaran, N.; Kotthaus, S.; Allen, L. Impact of city changes and weather on anthropogenic heat flux in Europe 1995–2015. *Urban Clim.* **2013**, *4*, 1–15. [CrossRef]
25. Block, A.; Keuler, K.; Schaller, E. Impacts of anthropogenic heat on regional climate patterns. *Geophys. Res. Lett.* **2004**, *31*, 2–5. [CrossRef]
26. Ma, S.; Pitman, A.; Hart, M.; Evans, J.P.; Haghdadi, N.; MacGill, I. The impact of an urban canopy and anthropogenic heat fluxes on Sydney's climate. *Int. J. Clim.* **2017**, *37*, 255–270. [CrossRef]
27. Yang, B.; Yang, X.; Leung, L.R.; Zhong, S.; Qian, Y.; Zhao, C.; Chen, F.; Zhang, Y.; Qi, J. Modeling the Impacts of Urbanization on Summer Thermal Comfort: The Role of Urban Land Use and Anthropogenic Heat. *J. Geophys. Res. Atmos.* **2019**, *124*, 6681–6697. [CrossRef]
28. Chow, W.T.; Salamanca, F.; Georgescu, M.; Mahalov, A.; Milne, J.M.; Ruddell, B.L. A multi-method and multi-scale approach for estimating city-wide anthropogenic heat fluxes. *Atmospheric Environ.* **2014**, *99*, 64–76. [CrossRef]
29. U.S.C. Bureau, U.S. Census Bureau QuickFacts: Los Angeles City, California, (n.d.). Available online: https://www.census.gov/quickfacts/losangelescitycalifornia (accessed on 2 August 2020).
30. Zheng, Y.; Weng, Q. High spatial- and temporal-resolution anthropogenic heat discharge estimation in Los Angeles County, California. *J. Environ. Manag.* **2018**, *206*, 1274–1286. [CrossRef] [PubMed]
31. Kusaka, H.; Kimura, F. Coupling a Single-Layer Urban Canopy Model with a Simple Atmospheric Model: Impact on Urban Heat Island Simulation for an Idealized Case. *J. Meteorol. Soc. Jpn.* **2004**, *82*, 67–80. [CrossRef]
32. Ryu, Y.-H.; Baik, J.-J.; Lee, S.-H. A New Single-Layer Urban Canopy Model for Use in Mesoscale Atmospheric Models. *J. Appl. Meteorol. Clim.* **2011**, *50*, 1773–1794. [CrossRef]
33. Chen, F.; Kusaka, H.; Bornstein, R.; Ching, J.; Grimmond, C.S.B.; Grossman-Clarke, S.; Loridan, T.; Manning, K.W.; Martilli, A.; Miao, S.; et al. The integrated WRF/urban modelling system: Development, evaluation, and applications to urban environmental problems. *Int. J. Clim.* **2011**, *31*, 273–288. [CrossRef]
34. Skamarock, W.C.; Klemp, J.B.; Duda, M.G.; Fowler, L.D.; Park, S.-H.; Ringler, T.D. A Multiscale Nonhydrostatic Atmospheric Model Using Centroidal Voronoi Tesselations and C-Grid Staggering. *Mon. Weather. Rev.* **2012**, *140*, 3090–3105. [CrossRef]
35. Morrison, H.; Thompson, G.; Tatarskii, V. Impact of Cloud Microphysics on the Development of Trailing Stratiform Precipitation in a Simulated Squall Line: Comparison of One- and Two-Moment Schemes. *Mon. Weather Rev.* **2009**, *137*, 991–1007. [CrossRef]
36. Dudhia, J. Numerical study of convection observed during the winter monsoon experiment using a mesoscale two dimensional model. *J. Atmos. Sci.* **1989**, *46*, 3077–3107. [CrossRef]
37. Mlawer, E.J.; Taubman, S.J.; Brown, P.D.; Iacono, M.J.; Clough, S.A. Radiative transfer for inhomogeneous atmospheres: RRTM, a validated correlated-k model for the longwave. *J. Geophys. Res. Space Phys.* **1997**, *102*, 16663–16682. [CrossRef]
38. Bretherton, C.S.; Park, S. A New Moist Turbulence Parameterization in the Community Atmosphere Model. *J. Clim.* **2009**, *22*, 3422–3448. [CrossRef]
39. Grell, G.A.; Freitas, S.R. A scale and aerosol aware stochastic convective parameterization for weather and air quality modeling. *Atmos. Chem. Phys. Discuss.* **2014**, *14*, 5233–5250. [CrossRef]
40. Monin, A.S.; Obukhov, A.M. Basic laws of turbulent mixing in the surface layer of the atmosphere, Contrib. Geophys. *Inst. Acad. Sci.* **1954**, *24*, 163–187.
41. Fry, J.A.; Xian, G.; Jin, S.; Dewitz, J.A.; Homer, C.G.; Yang, L.; Barnes, C.A.; Herold, N.D.; Wickham, J.D. Completion of the 2006 national land cover database for the conterminous united states. *Photogramm. Eng. Remote. Sens.* **2011**, *77*, 858–864.

42. Wickham, J.; Stehman, S.V.; Gass, L.; Dewitz, J.; Fry, J.A.; Wade, T.G. Accuracy assessment of NLCD 2006 land cover and impervious surface. *Remote. Sens. Environ.* **2013**, *130*, 294–304. [CrossRef]
43. Vahmani, P.; Jones, A.D.; Patricola, C.M. Interacting implications of climate change, population dynamics, and urban heat mitigation for future exposure to heat extremes. *Environ. Res. Lett.* **2019**, *14*, 084051. [CrossRef]
44. Jones, B.; O'Neill, B.C.; McDaniel, L.; McGinnis, S.; Mearns, L.O.; Tebaldi, C. Future population exposure to US heat extremes. *Nat. Clim. Chang.* **2015**, *5*, 652–655. [CrossRef]
45. Garfin, G.; Jardine, A.; Merideth, R.; Black, M.; LeRoy, S. *Assessment of Climate Change in the Southwest United States: A Report Prepared for the National Climate Assessment*; Island Press: Washington, DC, USA, 2013.
46. Gershunov, A.; Cayan, D.R.; Iacobellis, S.F. The Great 2006 Heat Wave over California and Nevada: Signal of an Increasing Trend. *J. Clim.* **2009**, *22*, 6181–6203. [CrossRef]
47. Hong, T.; Chen, Y.; Lee, S.H.; Piette, M.A. CityBES: A web-based platform to support city-scale building energy efficiency. *Urban Comput.* **2016**, *14*. [CrossRef]
48. Los Angeles County GIS Data Portal. Countywide Building Outlines—2014 (2014). Available online: https://geohub.lacity.org/datasets/57f5fc977d6a427a978003a6229ab5e7/ (accessed on 2 August 2020).
49. DataLA: Information, Insights, and Analysis from the City of Angels: Los Angeles—Open Data Portal. City of Los Angeles. Available online: https://data.lacity.org/ (accessed on 2 August 2020).
50. Crawley, D.B.; Lawrie, L.K.; Pedersen, C.O.; Winkelmann, F.C. EnergyPlus: Energy simulation program. *ASHRAE J.* **2000**, *42*, 49–56.
51. ASHRAE. *ANSI/ASHRAE/IES Standard 90.1-2010*; Pacific Northwest National Laboratory: Richland, WA, USA, 2010.

Publisher's Note: MDPI stays neutral with regard to jurisdictional claims in published maps and institutional affiliations.

© 2020 by the authors. Licensee MDPI, Basel, Switzerland. This article is an open access article distributed under the terms and conditions of the Creative Commons Attribution (CC BY) license (http://creativecommons.org/licenses/by/4.0/).